INORGANIC CHEMISTRY FRONTIERS

RESEARCH ARTICLE

View Article Online
View Journal | View Issue



Cite this: *Inorg. Chem. Front.*, 2024, **11**, 3626

# Mixed lanthanide–organic frameworks with borono groups for colorimetric detection of excess fluoride levels in rivers†

Hui Min, *[a] Zhuohang Zhu, [a] Meiyi Huang,[a] Junbao Zhou,[a] Nian Zhao[a] and Peng Cheng *[b]

Received 15th March 2024,
Accepted 5th May 2024

DOI: 10.1039/d4qi00630e

rsc.li/frontiers-inorganic

Chronic fluoride ($F^-$) toxicity has been endemic at least 25 countries around the world due to prolonged consumption of contaminated water, posing a great threat to human health. Rapid and convenient visual methods for $F^-$ ion detection are hence needed for public safety. In this work, we show a series of novel mixed lanthanide–organic frameworks, namely $\{[Eu_xTb_{2-x}(BIPA)_3(DMF)(H_2O)_3]\cdot 2DMF\cdot 3H_2O\}_n$ ($H_2BIPA$ = 5-boronoisophthalic acid; $x$ = 0, 0.12, 0.28, 0.30, 0.68, 1.04 and 2 for **1–7**, respectively), with abundant recognition sites of borono groups for convenient and visual detection of excess $F^-$ ions in river water. Wide linear range for $F^-$ ion detection can be obtained through systematic optimization of sensing materials. A rare double dynamic sensing process between $F^-$ ions and lanthanide–organic frameworks was clearly revealed though single-crystal X-ray diffraction and transient fluorescence techniques.



## 1. Introduction

As the fluoridation process of public drinking water and daily necessities accelerate, fluoride ions ($F^-$) have been of easy access in daily life and are beneficial to human health at low concentrations.[1,2] However, chronic overconsumption of $F^-$ ions will cause severe adverse effects such as dental and skeletal fluorosis, fracture-proneness, urolithiasis, and impaired thyroid.[3–6] According to World Health Organization (WHO) guidelines for drinking-water quality in 2004, the concentration limit of $F^-$ ions for drinking water should be no more than 1.5 mg $L^{-1}$ for preventing osteofluorosis.[7] Convenient and accurate visual detection of excess $F^-$ ion levels in drinking water is hence needed for public safety. Up to now, different methods have been developed for $F^-$ ion level determination, including fluorescence, use of electrodes, and chromatography.[8–10] Nevertheless, these methods either have complex operations and take a long time or are poor in stability and not convenient for on-site detection.

As multifunctional porous crystalline materials, luminescent metal–organic frameworks (MOFs) have been paid wide attention in chemical sensing not only because of their devisable architectures and abundant luminescence sites but also due to the advantages in the designability of size and energy level matching.[11–15] Lanthanide–organic frameworks (Ln–MOFs) stand out from these materials because they can also fully demonstrate the excellent luminescence properties of lanthanide metals, such as long lifetime and high spectral resolution.[16–20] Mixed Ln–MOFs constructed with multi-lanthanide centers can reduce systematic error and improve sensitivity because of their special self-calibration function through ratiometric dual output modes.[21–25] To realize accurate $F^-$ detection in drinking water, adding precise recognition sites to mixed Ln–MOFs can greatly improve the selectivity and anti-interference ability. To this end, 5-boronoisophthalic acid ($H_2BIPA$) was selected as a ligand for constructing mixed Ln–MOFs with europium ($Eu^{3+}$) and terbium ($Tb^{3+}$) ions for the following points: (i) in previous work, it has been found that $H_2BIPA$ can effectively sensitize the luminescence of $Eu^{3+}$ and $Tb^{3+}$ *via* the "antenna effect",[26–28] (ii) $H_2BIPA$ contains electron-deficient borono group, which may capture $F^-$ ions according to the well-known Lewis theory of acids and bases, (iii) the interaction between $F^-$ ions and $H_2BIPA$ may change the energy levels of the ligand, thereby changing the energy transfer path inside of Ln–MOFs, and thus regulating the fluorescence of Ln–MOFs and finally realizing the detection of $F^-$

[a]*Hubei Key Laboratory of Pollutant Analysis & Reuse Technology, College of Chemistry and Chemical Engineering, Hubei Normal University, Huangshi 435002, P. R. China. E-mail: minhui@hbnu.edu.cn*
[b]*Department of Chemistry, Key Laboratory of Advanced Energy Material Chemistry, Frontiers Science Center for New Organic Matter, Haihe Laboratory of Sustainable Chemical Transformations (Tianjin), College of Chemistry, Nankai University, Tianjin 300071, P. R. China. E-mail: pcheng@nankai.edu.cn*

†Electronic supplementary information (ESI) available: Crystallographic data of 7 (CCDC 2326600) and F@7 (CCDC 2326601), supplementary figures and tables. For ESI and crystallographic data in CIF or other electronic format see DOI: https://doi.org/10.1039/d4qi00630e

ions, and (iv) in previous work, it has been demonstrated that borono-functionalized Ln–MOFs can be used to detect $F^-$ ions, but detailed crystal data and $F^-$ capture process have not been clearly reported.[28]

In this work, a series of novel Ln–MOFs, $\{[Eu_xTb_{2-x}(BIPA)_3(DMF)(H_2O)_3]\cdot 2DMF\cdot 3H_2O\}_n$ ($Eu_xTb_{2-x}$–MOF; $x$ = 0, 0.12, 0.28, 0.30, 0.68, 1.04 and 2 for **1–7**, respectively; DMF: *N*,*N*-dimethylformamide), were synthesized and characterized in detail for highly efficient visual detection of $F^-$ ions. Isomorphic $Gd_2$–MOF (**8**) was synthesized for energy level studies. After the stepwise optimization of sensing materials, **5** was screened out for $F^-$ ion detection and displays high sensitivity, excellent selectivity, and a low limit of detection (LOD) of 0.165 ppm. The best sensing performance of **5** may be due to its highest intramolecular energy transfer efficiency ($E$) from $Tb^{3+}$ to $Eu^{3+}$ ions. The further detection of $F^-$ ions in actual water samples from a river show that **5** can be used in practice.

# 2. Experimental

## 2.1. Materials and methods

All chemicals purchased were of reagent grade and used without further purification. The single-crystal data of **7** and F@7 were collected using a Rigaku XtaLAB Mini II single-crystal diffractometer equipped with graphite–monochromatic Mo-Kα radiation ($\lambda$ = 0.71073 Å). Structures were solved by SHELXS (direct methods) and refined by SHELXL (full matrix least-squares techniques) in the *Olex 2* package.[29,30] Powder X-ray diffraction (PXRD) experiments were performed using a Bruker D2 PHASER diffractometer with Cu-Kα radiation ($\lambda$ = 1.54186 Å) through scanning over the range of 5–50° at a scan rate of 0.2° $s^{-1}$ at room temperature. Simulations of PXRD patterns were carried out with the single-crystal data and diffraction crystal module of the Mercury program available free of charge *via* **https://www.ccdc.cam.ac.uk/mercury/**. Thermogravimetric analysis (TGA) was carried out with a NETZSCH STA 449F5 (TG/DTA) thermal analyzer under nitrogen flow. Fourier transform infrared spectroscopy (FTIR) was conducted using a Bruker AXS TENSOR-27 FTIR spectrometer with pressed KBr pellets in the range of 4000–400 $cm^{-1}$. Elemental analysis (EA) for C, H and N was carried out using a Vario EL cube elemental analyzer. Inductively coupled plasma-atomic emission spectrometry (ICP-AES) analyses were conducted using an Agilent 7900 instrument. Ultraviolet–visible (UV-vis) absorption spectra were measured with a Hitachi U-3010 UV-vis spectrophotometer. X-ray photoelectron spectroscopy (XPS) data were acquired using a Thermo Scientific K-Alpha instrument. Luminescence spectra were recorded using an Edinburgh FS5 fluorescence spectrophotometer equipped with a xenon lamp and pulsed flash lamp at room temperature. Photos were taken with a HUAWEI Nova 8 pro under 278 nm excitation of a Hitachi RF6000 fluorescence spectrometer. The $F^-$ ion selective electrode (PF-1Q9) was purchased from Shanghai Ruosull Technology Co. Ltd.

## 2.2. Synthesis

$H_2BIPA$ (0.1 mmol, 0.021 g), pinacol (0.1 mmol, 0.012 g), 1 mL DMF and 4 mL $H_2O$ were added to a 20 mL glass bottle to form a solution under ultrasound. Then, 1 mL of europium acetate tetrahydrate ($Eu(AC)_3\bullet 4H_2O$) aqueous solution (0.1 mol $L^{-1}$) was added. The glass bottle was sealed and heated at 90 °C for 24 h, and colorless crystals (**7**) were formed at the bottom of the glass bottle. **7** was collected by filtration and washed with distilled water three times and then dried in air. **1–6** were obtained using a similar method to that for **7** by replacing $Eu(AC)_3$ aqueous solution with terbium/europium/gadolinium acetate aqueous solution with different volumes (1 mL in total). Yield: 41%, 38%, 33%, 31%, 33%, 35%, 34% and 36% based on $H_2BIPA$ for **1–8**, respectively. The feed volume and chemical composition of **1–7** were further confirmed by ICP-AES and EA (Table S1†). F@7 was obtained after treating **7** with an aqueous solution with 33 ppm $F^-$ ions at 80 °C for 12 h.

## 2.3. Luminescence measurements

Finely ground lanthanide MOFs (**1–7**) (10 mg) were dispersed into distilled water (50 mL) to form aqueous suspensions, which were then sonicated for 5 min. Luminescence spectra upon excitation at 278 nm were measured *in situ* after incremental addition of freshly prepared analyte solutions to a 3 mL suspension of **1–7**. For selectivity and anti-interference experiments, aqueous suspensions were similarly prepared, with addition of 50 μL of 1 mmol $L^{-1}$ aqueous solution of NaCl, NaBr, KBr, KOCN, KSCN, KSeCN, $BaCl_2$, $CaCl_2$, $MnCl_2$, $Na_2SO_4$, $NiCl_2$, $SrCl_2$, $MgCl_2$ and/or 31.2 ppm NaF into the aqueous suspensions of **5**.

## 2.4. Experiments for actual water samples

As-obtained water samples from Yangtze River (1–3) were treated by centrifugation at 10 000 rpm for 5 min to obtain clear liquids at the top of centrifuge tubes for direct spike-and-recovery experiments using **5**. The same batch of samples were also used for $F^-$ ion detection by $F^-$ ion selective electrode for comparation. Saturated calomel electrode was used as the reference electrode. Seven standard solutions including $10^{-1}$, $10^{-2}$, $10^{-3}$, $10^{-4}$, $10^{-5}$, and $10^{-6}$ M NaF standard solution was used for obtaining a standard curve for actual water sample detection.

# 3. Results and discussion

## 3.1. Structural description and characterizations

**1–8** are crystallized in the $P\bar{1}$ space group through a fast self-assembly process of lanthanide ions and $H_2BIPA$ under solvothermal conditions (Table S2†). Their crystal structure can be hence described in detail using **7** as a representative. The minimum asymmetric unit of **7** includes three $BIPA^{2-}$, two $Eu^{3+}$ ions, three coordination water molecules, a coordination DMF molecule and series of lattice species. Two crystallographically independent $Eu^{3+}$ ions are in eight-coordination (Eu1)

and nine-coordination (Eu2) modes with oxygen atoms, forming biaugmented trigonal prism and muffin configuration, respectively (Fig. 1a, and Table S3†). Two congeneric $Eu^{3+}$ ions are linked by four $\mu_2$–$\eta^1$:$\eta^1$ carboxyl groups of four $BIPA^{2-}$ to form a binuclear $\{Eu_2\}$ unit, and each $BIPA^{2-}$ is connected to two $\{Eu_2\}$ units to form a two-dimensional network in the *ac* plane (Fig. 1b), which is further connected into a three-dimensional framework through two $\mu_1$–$\eta^1$:$\eta^1$ carboxyl groups of $BIPA^{2-}$ (Fig. 1c). The topology of **7** can be simplified into *pcu* configuration by taking two kinds of six-connected $\{Eu_2\}$ units as nodes (Fig. 1d and Fig. S1†).

The PXRD patterns show that the diffraction peaks of as-synthesized compounds match well with simulated peaks from the single-crystal data of **7** (Fig. S2†). In addition, these isomorphic crystals displayed similar FTIR curves, confirming their phase purity (Fig. S3†). MOFs with great water stability should possess strong coordination bonds (thermodynamic stability) or significant steric hindrance (kinetic stability) to prevent the hydrolysis reaction that breaks metal–ligand bonds.[31–33] For Ln–MOFs, Ln–O coordination bonds are relatively weak, and thus, it is desired to obtain the appropriate chelating model of ligands to form a rigid structure to prevent attack of water molecules.[34] As is shown in Fig. S4,† the diffraction peaks of **7** after immersion in water for 48 hours are in good agreement with those of the original compound, revealing its high water stability. The TGA of **7** was conducted in the temperature range of 40–800 °C (Fig. S5†). A clear weight loss of 4.75% was observed in the range of 40–102 °C, keeping up with the loss of three lattice water molecules (cal. 4.60%). Obvious weight loss of 11.92% was observed at 102–256 °C, agreeing with the loss of two lattice DMF molecules (cal. 11.47%). The loss of coordinated solvent molecules was observed before 427 °C, and further heating-induced sharp weight losses were attributed to the decomposition of the frameworks.

### 3.2. Luminescent detection of $F^-$ ions

The solid-state luminescence emission spectra of **1–7** were investigated with an excitation wavelength of 287 nm (Fig. 2a). Typically, **7** and **1** displayed characteristic emission peaks at 579, 592, 616, 652, 697 nm ($^5D_0 \rightarrow {}^7F_J$, $J$ = 0, 1, 2, 3, 4) and 489, 545, 585, 621 nm ($^5D_4 \rightarrow {}^7F_J$, $J$ = 6, 5, 4, 3), respectively, while **2–6** show the characteristic emission peaks of the $Eu^{3+}$ and $Tb^{3+}$ ions, indicating the successful mixing of $Eu^{3+}$ and $Tb^{3+}$. **1–7** display seven different gradient luminescence colors from green to red (Fig. 2a, inset), and **7** displays rare pure red color according to its *CIE-1931* chromaticity coordinates (Fig. 2b). The lifetimes of $Tb^{3+}$ and/or $Eu^{3+}$ in **1–7** were determined to investigate the energy transfer efficiency ($E$) between $Tb^{3+}$ and $Eu^{3+}$ according to the equation of $E = 1 - \tau_n/\tau_1$, where $\tau_n$ is the lifetime of $Tb^{3+}$ in **1–6** (Fig. 2c). With an increase of Eu content, the $E$ value first increases and further decreases, and **5** shows the highest $E$ value of 29.8% (Fig. 2d).

The aqueous dispersions of **1–7** display similar luminescence emission spectra to those of their crystalline states (Fig. S6†), and their luminescence intensity remained constant for 15 minutes (Fig. S7†), indicating they are suitable for luminescent detection in water. Luminescent titrations of $F^-$ ions were performed using aqueous dispersions of **1–7** (Fig. S8 and S9†). With the concentration of $F^-$ ions increasing from 0 to 31.7 ppm, all intensities ($I$) at 544 and/or 616 nm for the seven compounds decreased (Fig. 3a), which obeyed the Stern–Volmer (S–V) equation: $I_0/I = K_{SV}[C] + 1$ in the low concentration ($[C]$) range of $F^-$ ions, where $K_{SV}$ is the quenching constant (Fig. S9 and S10†). $K_{SV}$ values fitted by intensities at 544

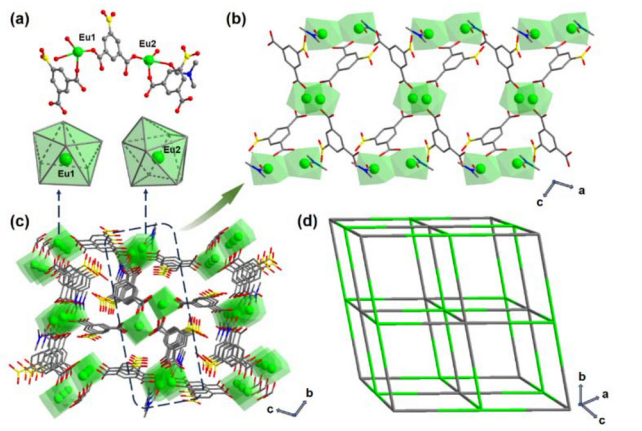


**Fig. 1** (a) Minimum asymmetric unit of **7** and coordination configuration of the $Eu^{3+}$ ions. (b) Connection of binuclear $Eu_2$ units and $BIPA^{2-}$ in the *ac* plane. (c) Three-dimensional framework of **7** in the *bc* plane. (d) Simplified *pcu* topological configuration of **7**. Atoms: Eu (green), C (gray), O (red), N (blue), B (yellow); H atoms are omitted for simplification.

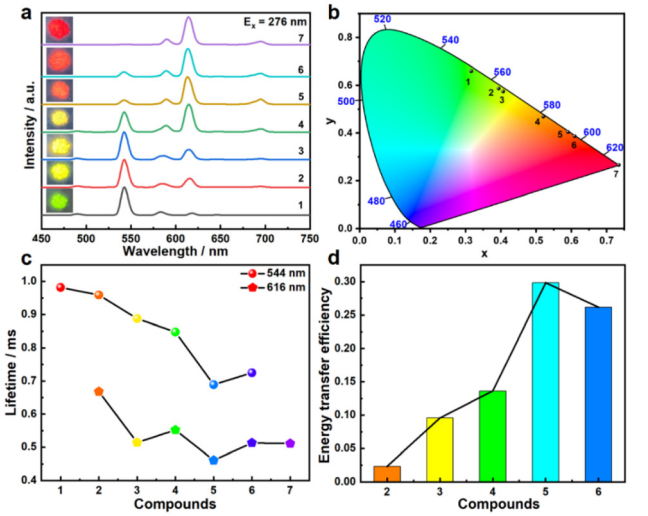


**Fig. 2** Solid-state luminescence emission spectra (a) and *CIE-1931* chromaticity coordinates (b) of **1–7**. Insets of (a) show solid luminescence pictures of **1–7** under 365 nm ultraviolet light. (c) Solid luminescence lifetimes of **1–7** at 544 and/or 616 nm. (d) Energy transfer efficiencies of **2–6**.

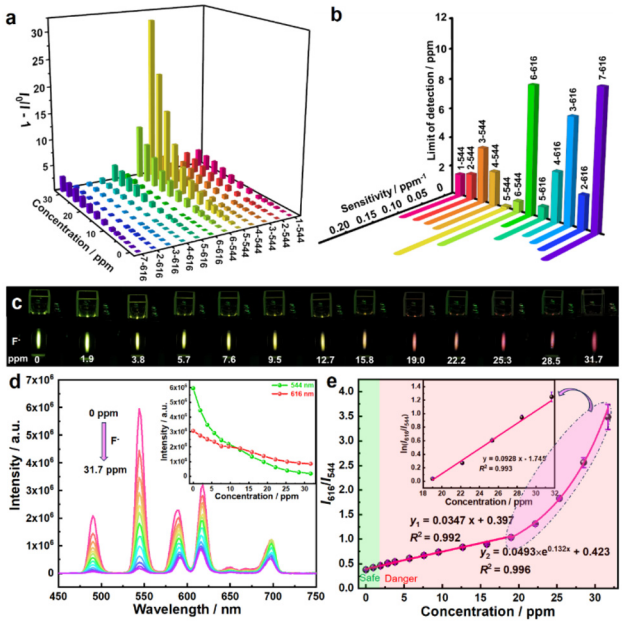


**Fig. 3** (a) Stern–Volmer (S–V) plots of **1–7** at 544/616 nm vary with the concentration of $F^-$ ions. (b) Sensing performance summary of **1–7** using intensities at 544 and/or 616 nm. (c) *In situ* color changes of **5** aqueous dispersion towards $F^-$ ions with different concentrations. (d) Luminescence response of **5** aqueous dispersion towards $F^-$ ions with different concentrations; inset shows the trend of change of luminescence intensity at 544 nm and 616 nm. (e) Intensity ratio ($I_{616}/I_{544}$) of 616 nm and 544 nm varies with the concentration of $F^-$ ions; inset shows the logarithmic relationship between $I_{616}/I_{544}$ and concentration at high concentration range. All data points of (d) and (e) are the average values of three measurements, and error bars show the 95% confidence interval.

and/or 616 nm of **1–7** were 0.0837, 0.0787/0.0546, 0.0793/0.0423, 0.0856/0.0289, 0.183/0.166, 0.125/0.739, and 0.0776 ppm$^{-1}$, respectively. With a further increase of concentration, all S–V points showed typical exponential function relationships: $I_0/I = a \times e^{b[C]} + c$, where $a$, $b$ and $c$ are constants. This phenomenon might be attributed to a self-absorption or energy transfer process.[35] The LODs of **1–7** are 1.5, 1.73/2.28, 3.74/7.03, 2.31/3.33, 0.166/0.83, 0.739/8.54 and 9.15 ppm, respectively, based on the 3$\sigma$ IUPAC criteria.[36]

The sensing performances including sensitivity and LOD of **1–7** are summarized and compared in Fig. 3b and Table S4.† **5** obviously behaved best and was screened out for further study. The reason for the best performance of **5** may be attributed to the highest $E$ value from $Tb^{3+}$ to $Eu^{3+}$ ions discussed above. The higher the $E$ value, the easier it is to influence through interacting with analyte ($F^-$ ion), thus realizing higher sensitivity. Considering that there are two different emission centers ($Eu^{3+}$ and $Tb^{3+}$) in **5**, the ratiometric $F^-$ ion detection behaviour was studied in detail. *In situ* titration experiment of **5** gives gradual changes of luminescence color from green to yellow and ultimately to red towards $F^-$ ions from 0 to 31.7 ppm (Fig. 3c). As the concentration of $F^-$ ions increases, the fluorescence intensity at 544 nm decreased rapidly, while that at 616 nm decreased slowly (Fig. 3d). The difference in reduction in luminescence intensity at 544 and 616 nm may be attributed to the energy transfer process of $Tb^{3+}$ to $Eu^{3+}$ ions in **5**.[26] The intensity ratio ($I_{616}/I_{544}$) of 616 nm and 544 nm showed two different response behaviours (Fig. 3e): (i) when the concentration of $F^-$ ions is less than 19 ppm, $I_{616}/I_{544}$ is linearly dependent on $F^-$ ion concentration with the relationship of $y = 0.0347x + 0.397$; (ii) when the concentration of $F^-$ ions is higher than 19 ppm, a clear exponential relationship of $y = 0.0493 \times e^{0.132x} + 0.423$ between $I_{616}/I_{544}$ and $F^-$ ion concentration was found. These results indicate that there are two distinct interactions between **5** and $F^-$ ions. The LOD in this situation is 0.68 ppm, which is lower than the specified risk concentration (1.5 ppm) of $F^-$ ions in water set by the WHO, indicating that **5** has potential applications for $F^-$ ion detection in water.

Before practical application, the selectivity and anti-interference ability of **5** towards $F^-$ ions were explored. After adding the major components of drinking water and some pseudo halogen ions, including NaCl, NaBr, KBr, KOCN, KSCN, KSeCN, $BaCl_2$, $CaCl_2$, $MnCl_2$, $Na_2SO_4$, $NiCl_2$, $SrCl_2$ and $MgCl_2$ (1 mmol L$^{-1}$, 50 μL), the fluorescence of **5** dispersion remained green and $I_{616}/I_{544}$ changed little, but it increased sharply, and the fluorescence turned to red when 31.2 ppm NaF was added (Fig. 4a and b). These results indicate that **5** shows excellent selectivity for $F^-$ ions. Besides, when these metal salts coexist with NaF, $I_{616}/I_{544}$ is roughly equal to that for NaF only (Fig. 4c), indicating that **5** displays satisfactory anti-interference ability for $F^-$ ion detection. To verify the practical application ability, water samples from the Yangtze River were used for spike-and-recovery experiments, which show recoveries in the range of 97.0%–98.0%, confirming that **5** can be used for $F^-$ ion detection in real samples (Table S5†). To verify the detection accuracy in this work, the same batch of samples were also used for detection of $F^-$ ions using the well-known methods such as $F^-$ ion selective electrodes (Fig. S11†). Detection results show that $F^-$ ion concentrations in different river samples were all about 0.80 ppm, which were relatively

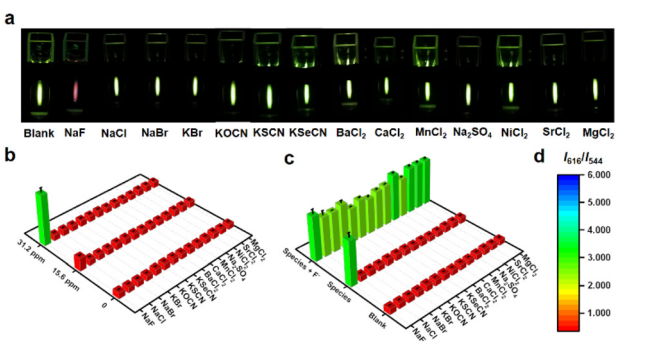


**Fig. 4** (a) Pictures of **5** aqueous dispersion before and after adding different interfering species. Selectivity (b), anti-interference (c) and colormap (d) of **5** toward $F^-$ ions in common ions. All data points are the average values of three measurements, and error bars show the 95% confidence interval.

coincident with the detection results using **5**. In addition, the results of tests using **5** after adding standard $F^-$ ion solution show lower standard deviation.

### 3.3. Sensing mechanism study

The detailed sensing mechanism was revealed by a series of spectroscopic studies and single-crystal structure analysis. The PXRD peaks of **5** before and after $F^-$ ion treatment are consistent with the simulated peaks, indicating that $F^-$ ions will not destroy the framework of **5** (Fig. S12†). The sensing of $F^-$ ions is therefore caused by host–guest interactions. Compared with bonding energy of B 1s in **5** in view of XPS spectra, small changes (from 190.86 to 190.70 eV) can be found after treating **5** with $F^-$ ions, indicating weak interactions exit between B atoms and $F^-$ ions (Fig. S13†). These results are similar to those reported in the literature.[8,26] Besides, new FTIR peaks at 706 and 750 $cm^{-1}$ formed, which may be caused by the formation of B···F interaction (Fig. S14†).[37,38] Considering that **7** and **5** are isomorphic, the interactions of **5** and $F^-$ ions should be similar to those of **7** and $F^-$ ions. Hence, the formed B···F interaction can be observed by comparing single-crystal X-ray diffraction results of **7** and F@**7** (Fig. 5a and Table S2†). The interaction distance of B···F is about 1.628 Å, which is longer than the traditional B–F bond length (about 1.38 Å). This result is consistent with the conclusion that weak interaction between borono group and $F^-$ ions exists, which may be caused by the steric effect of water molecules interacting with borono group though hydrogen bond interactions. This interaction is different from electrostatic interaction between $F^-$ ions and Ln–MOF or high affinity nature between $F^-$ ions and $Ln^{3+}$ ions.[8,39] The singlet energy level and triplet energy level of the ligand are 41 152 and 22 936 $cm^{-1}$, respectively, which are suitable for sensitization of the $Eu^{3+}$ and $Tb^{3+}$ ions (Fig. S15†). With $F^-$ ion concentration increasing, weak changes in UV-vis absorption spectra can be observed, indicating the singlet energy level of the ligand can be influenced by $F^-$ ions (Fig. S16†). As a result, the energy transfer process within **5** changes, eventually causing a change in luminescent color. This conclusion was further verified by transient fluorescence spectra of **5** before and after treating with $F^-$ ions (Fig. S17 and S18†). As the concentration of $F^-$ ions increases, the lifetime at 544 nm decreases first and later increases, while the lifetime at 616 nm increases all the way (Fig. 5b and c, S19 and Table S6†). The opposite changes in the fluorescence lifetimes of the $Tb^{3+}$ and $Eu^{3+}$ ions at the beginning not only indicate dynamic interactions between **5** and $F^-$ ions but also indicate that $F^-$ ions accelerate the energy transfer from the $Tb^{3+}$ to $Eu^{3+}$ ions under unacted saturated state. With the further increase of $F^-$ ion concentration, the lifetimes of $Eu^{3+}$ ion and $Tb^{3+}$ ion increase simultaneously, indicating that the interactions between $F^-$ ions and **5** can improve the energy transfer efficiency from ligand to $Tb^{3+}/Eu^{3+}$ ions after saturation.

Hence, the sensing mechanism can be summarized as follows (Fig. 5d): under 278 nm excitation, luminescence the of $Eu^{3+}$ and $Tb^{3+}$ ions can be emitted through the traditional "antenna effect" process. After a weak interaction between the ligand and $F^-$ ions, the energy transfer from the $Tb^{3+}$ to $Eu^{3+}$ ions accelerates, and the linear change of $I_{616}/I_{544}$ is induced with a slow color change. After saturation of this interaction, the energy transfer efficiency from ligand to $Tb^{3+}/Eu^{3+}$ ions is promoted, causing the exponential growth of $I_{616}/I_{544}$ with a fast color change.

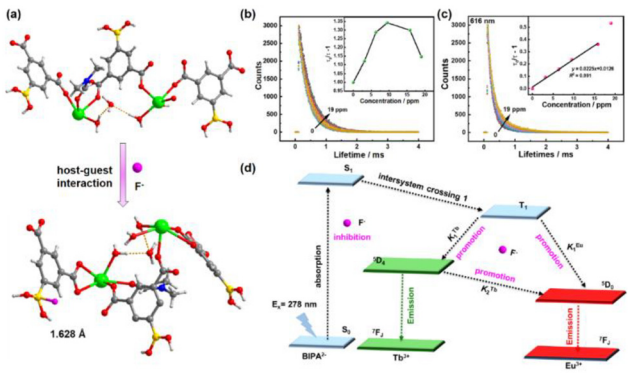


**Fig. 5** (a) Host–guest interaction between **5** and $F^-$ ions. Transient fluorescence spectra of **5** at 544 nm (b) and 616 nm (c) before and after treating with $F^-$ ions; insets show the lifetime-based S–V points and their change tendency or fitted result. (d) Energy transfer mechanism diagram.

## 4. Conclusions

In summary, we synthesized and characterized a family of lanthanide metal–organic frameworks with borono groups, which can be used for visual detection of $F^-$ ions through the change of luminescence color from green to red. Through a series of spectral studies and crystal structure analysis, rare double dynamic interactions between $F^-$ and lanthanide metal–organic frameworks have been revealed in detail, to give a deep understanding of double response relationships between fluorescence intensity ratio and concentration at low and high concentrations. The $F^-$ ion response mechanism is thoroughly analyzed from the perspective of host–guest interaction, which provides new insights for the design, synthesis and application of MOF-based sensing materials for environmental pollutants.

## Author contributions

H. M. designed the experiments, analyzed experimental data and completed the manuscript. Z. Z., M. H., and J. Z. did experiments. H. M., N. Z. and P. C. discussed the idea and polished the manuscript.

## Conflicts of interest

There are no conflicts to declare.

## Acknowledgements

This work is supported by the National Natural Science Foundation of China (grant number 22121005), open-ended fund of Hubei Key Laboratory of Pollutant Analysis & Reuse Technology (grant number PA230212) and talent introduction project of Hubei Normal University (grant number HS2023RC072).

## References

1 J. D. B. Featherstone, Prevention and reversal of dental caries: Role of low level fluoride, *Community Dent. Oral Epidemiol.*, 1999, **27**, 31–40.
2 S. Roy and G. Dass, Fluoride contamination in drinking water–a review, *Resour. Environ.*, 2013, **3**, 53–58.
3 L. S. Kaminsky, M. C. Mahoney, J. Leach, J. Melius and M. J. Miller, Fluoride: benefits and risks of exposure, *Crit. Rev. Oral Biol. Med.*, 1990, **1**, 261–281.
4 D. L. Ozsvath, Fluoride and environmental health: a review, *Rev. Environ. Sci. Biotechnol.*, 2009, **8**, 59–79.
5 S. Ayoob and A. K. Gupta, Fluoride in drinking water: a review on the status and stress effects, *Crit. Rev. Environ. Sci. Technol.*, 2006, **36**, 433–487.
6 Z. Kheradpisheh, M. Mirzaei, A. H. Mahvi, M. Mokhtari, R. Azizi, H. Fallahzadeh and M. H. Ehrampoush, Impact of drinking water fluoride on human thyroid hormones: a case–control study, *Sci. Rep.*, 2018, **8**, 2674.
7 World Health Organization, *WHO 2004 Guidelines for drinking-water quality*, Geneva, 3rd edn.
8 F. M. Ebrahim, T. N. Nguyen, S. Shyshkanov, A. Gładysiak, P. Favre, A. Zacharia, G. Itskos, P. J. Dyson and K. C. Stylianou, Selective, fast-response, and regenerable metal–organic framework for sampling excess fluoride levels in drinking water, *J. Am. Chem. Soc.*, 2019, **141**, 3052–3058.
9 J. Shen, S. Gagliardi, M. R. S. McCoustra and V. Arrighi, Effect of humic substances aggregation on the determination of fluoride in water using an ion selective electrode, *Chemosphere*, 2016, **159**, 66–71.
10 M. A. G. T. van den Hoop, R. F. M. J. Cleven, J. J. van Staden and J. Neele, Analysis of fluoride in rain water comparison of capillary electrophoresis with ion chromatography and ion–selective electrode potentiometry, *J. Chromatogr. A*, 1996, **739**, 241–248.
11 S. Wu, H. Min, W. Shi and P. Cheng, Multicenter metal–organic framework–based ratiometric fluorescent sensors, *Adv. Mater.*, 2020, **32**, 1805871.
12 Y. Zhang, S. Yuan, G. Day, X. Wang, X. Yang and H.-C. Zhou, Luminescent sensors based on metal-organic frameworks, *Coord. Chem. Rev.*, 2018, **354**, 28–45.
13 J. Hao, X. Xu, H. Fei, L. Li and B. Yan, Functionalization of metal–organic frameworks for photoactive materials, *Adv. Mater.*, 2018, **30**, 1705634.
14 Y. Cui, J. Zhang, H. He and G. Qian, Photonic functional metal–organic frameworks, *Chem. Soc. Rev.*, 2018, **47**, 5740–5785.
15 W. P. Lustig, S. Mukherjee, N. D. Rudd, A. V. Desai, J. Li and S. K. Ghosh, Metal–organic frameworks: functional luminescent and photonic materials for sensing applications, *Chem. Soc. Rev.*, 2017, **46**, 3242–3285.
16 J. Rocha, L. D. Carlos, F. A. Almeida Paz and D. Ananias, Luminescent multifunctional lanthanides–based metal–organic frameworks, *Chem. Soc. Rev.*, 2011, **40**, 926–940.
17 P. Cheng, *Lanthanides: Fundamentals and applications [M]*, Elsevier, 2023.
18 F. Saraci, V. Quezada-Novoa, P. R. Donnarumma and A. J. Howarth, Rare-earth metal–organic frameworks: from structure to applications, *Chem. Soc. Rev.*, 2020, **49**, 7949–7977.
19 X. Zhang, H. Qiu, W. Luo, K. Huang, Y. Chen, J. Zhang, B. Wang, D. Peng, Y. Wang and K. Zheng, High–performance *X*–ray Imaging using lanthanide metal–organic frameworks, *Adv. Sci.*, 2023, **10**, 2207004.
20 X. Wang, Y. Jiang, A. Tissot and C. Serre, Luminescent sensing platforms based on lanthanide metal-organic frameworks: Current strategies and perspectives, *Coord. Chem. Rev.*, 2023, **497**, 215454.
21 L. Chen, D. Liu, J. Peng, Q. Du and H. He, Ratiometric fluorescence sensing of metal-organic frameworks: Tactics and perspectives, *Coord. Chem. Rev.*, 2020, **404**, 213113.
22 S. Abednatanzi, P. G. Derakhshandeh, H. Depauw, F.-X. Coudert, H. Vrielinck, P. V. D. Voort and K. Leus, Mixed–metal metal–organic frameworks, *Chem. Soc. Rev.*, 2019, **48**, 2535–2563.
23 S.-Y. Zhang, W. Shi, P. Cheng and M. J. Zaworotko, A mixed–crystal lanthanide zeolite–like metal–organic framework as a fluorescent indicator for lysophosphatidic acid, a cancer biomarker, *J. Am. Chem. Soc.*, 2015, **137**, 12203–12206.
24 F. Chen, Y.-M. Wang, W. Guo and X.-B. Yin, Color-tunable lanthanide metal–organic framework gels, *Chem. Sci.*, 2019, **10**, 1644–1650.
25 X.-Y. Wang, X. Yao, Q. Huang, Y.-X. Li, G.-H. An and G.-M. Li, Triple–wavelength–region luminescence sensing based on a color–tunable emitting lanthanide metal organic framework, *Anal. Chem.*, 2018, **90**(11), 6675–6682.
26 H. Min, Z. Chen, Z. Han, K. Wang, J. Xu, W. Shi and P. Cheng, Detection of the UV-vis silent biomarker trimethylamine-*N*-oxide via outer-sphere interactions in a lanthanide metal-organic framework, *Commun. Chem.*, 2022, **5**, 74.
27 Y.-M. Wang, Z.-R. Yang, L. Xiao and X.-B. Yin, Lab-on-MOFs: Color-coded multitarget fluorescence detection with white-light emitting metal–organic frameworks under single wavelength excitation, *Anal. Chem.*, 2018, **90**, 5758–5763.
28 Z.-R. Yang, M.-M. Wang, X.-S. Wang and X.-B. Yin, Boric-acid-functional lanthanide metal–organic frameworks for

selective ratiometric fluorescence detection of fluoride ions, *Anal. Chem.*, 2017, **89**, 1930–1936.

29 O. V. Dolomanov, L. J. Bourhis, R. J. Gildea, J. A. K. Howard and H. Puschmann, *OLEX2*: a complete structure solution, refinement and analysis program, *J. Appl. Crystallogr.*, 2009, **42**, 339–341.

30 G. M. Sheldrick, Crystal structure refinement with *SHELXL*, *Acta Crystallogr., Sect. C: Struct. Chem.*, 2015, **71**, 3–8.

31 N. C. Burtch, H. Jasuja and K. S. Walton, Water stability and adsorption in metal–organic frameworks, *Chem. Rev.*, 2014, **114**, 10575–10612.

32 A. J. Howarth, Y. Liu, P. Li, Z. Li, T. C. Wang, J. T. Hupp and O. K. Farha, Chemical, thermal and mechanical stabilities of metal–organic frameworks, *Nat. Rev. Mater.*, 2016, **1**, 15018.

33 S. Yuan, L. Feng, K. Wang, J. Pang, M. Bosch, C. Lollar, Y. Sun, J. Qin, X. Yang, P. Zhang, Q. Wang, L. Zou, Y. Zhang, L. Zhang, Y. Fang, J. Li and H.-C. Zhou, Stable metal–organic frameworks: Design, synthesis, and applications, *Adv. Mater.*, 2018, **30**, 1704303.

34 H. Min, Z. Han, T. Sun, K. Wang, J. Xu, P. Yao, S. Yang, P. Cheng and W. Shi, Dynamic–static coupled sensing of trace biomarkers by molecularly imprinted metal–organic frameworks, *Sci. China: Chem.*, 2023, **66**, 3511–3517.

35 H. Min, S. Wu, Z. Han, Z. Chen, T. Sun, W. Shi and P. Cheng, Fast detection of entacapone by a lanthanide–organic framework with rhombic channels, *Chem. – Eur. J.*, 2021, **27**, 17459–17464.

36 Analytical Methods Committee, Recommendations for the definition, estimation and use of the detection limit, *Analyst*, 1987, **112**, 199–204.

37 R. Hattori, E. Suzuki and K. Shimizu, Matrix isolation FTIR and DFT studies of methyl isocyanide-boron trifluoride complex, *J. Mol. Struct.*, 2005, **738**, 165–170.

38 P. O. Ike, D. E. Folley, C. D. Umeh, K. K. Agwu, M. L. Chithambo, S. Chikwembani and F. I. Ezema, The effect of copper on the structural and thermoluminescence properties of aluminium borate, *J. Lumin.*, 2020, **226**, 117504.

39 X. Zeng, J. Hu, M. Zhang, F. Wang, L. Wu and X. Hou, Visual detection of fluoride anions using mixed lanthanide metal–organic frameworks with a smartphone, *Anal. Chem.*, 2020, **92**, 2097–2102.

 